Author for correspondence:
Stephen G. Warren
e-mail: sgw@uw.edu

Optical properties of ice and snow

Stephen G. Warren

Department of Atmospheric Sciences, University of Washington, PO Box 351640, Seattle, WA 98195, USA

SGW, 0000-0001-5429-7100

The interactions of electromagnetic radiation with ice, and with ice-containing media such as snow and clouds, are determined by the refractive index and absorption coefficient (the 'optical constants') of pure ice as functions of wavelength. Bulk reflectance, absorptance and transmittance are further influenced by grain size (for snow), bubbles (for glacier ice and lake ice) and brine inclusions (for sea ice). Radiative transfer models for clouds can also be applied to snow; the important differences in their radiative properties are that clouds are optically thinner and contain smaller ice crystals than snow. Absorption of visible and near-ultraviolet radiation by ice is so weak that absorption of sunlight at these wavelengths in natural snow is dominated by trace amounts of light-absorbing impurities such as dust and soot. In the thermal infrared, ice is moderately absorptive, so snow is nearly a blackbody, with emissivity 98–99%. The absorption spectrum of liquid water resembles that of ice from the ultraviolet to the mid-infrared. At longer wavelengths they diverge, so microwave emission can be used to detect snowmelt on ice sheets, and to discriminate between sea ice and open water, by remote sensing. Snow and ice are transparent to radio waves, so radar can be used to infer ice-sheet thickness.

This article is part of the theme issue 'The physics and chemistry of ice: scaffolding across scales, from the viability of life to the formation of planets'.

1. Introduction

The optical properties of ice and snow are important for the energy budgets of solar and infrared radiation, and therefore the climate, over large parts of the Earth's surface. The optical properties are also used to explain and predict photochemistry in snow, and they

THE ROYAL SOCIETY PUBLISHING
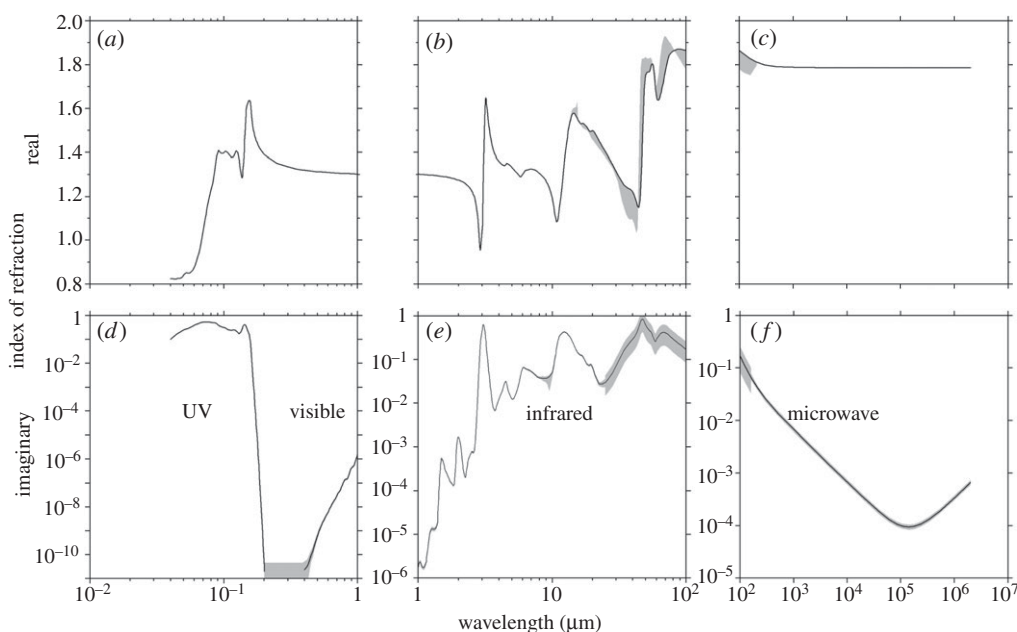
Figure 1. Compilation of the real and imaginary parts of the complex index of refraction of ice Ih at temperature 266 K. The shading indicates uncertainty. Modified from fig. 9 of Warren & Brandt [4].

are needed for designing remote-sensing instruments on satellites and for interpreting the remote-sensing measurements. We start this perspective with the radiative properties of pure hexagonal ice, namely the 'optical constants', as functions of wavelength.

2. Optical constants of ice

The dominant absorption mechanisms for ice are electronic in the ultraviolet (UV), molecular vibration in the near-infrared (near-IR), hindered rotation in the thermal IR and lattice translations in the far-IR. In weakly absorbing spectral regions, the absorption coefficient is measured by transmission (e.g. [1]); in strong bands, by reflection (e.g. [2]). The absorption coefficient and refractive index are combined as the complex index of refraction $m = m_{re} + i m_{im}$, where m_{im} is related to the linear absorption coefficient k_a as

$$k_a = \frac{4\pi m_{im}}{\lambda}. \tag{2.1}$$

Laboratory measurements use different methods in the different wavelength domains, so individual publications usually cover only a restricted spectral band. A compilation of these measurements was made by Warren [3], covering all wavelengths from the UV to the microwave (wavelengths 40 nm to 2 m); it was superseded by a revised compilation by Warren & Brandt [4] (hereafter WB08). Figure 1 shows this revised compilation, for ordinary hexagonal ice Ih at temperature 266 K (in fact this entire review will almost exclusively concern ice Ih).

(a) Absorption bands

There are several things to note in figure 1. The real index oscillates in the narrow range of approximately 1–2, whereas the imaginary index varies by ten orders of magnitude. (In regions of very strong absorption, where the mean free path of a photon is smaller than the wavelength, m_{re} can drop below 1.0, as at $\lambda < 70$ nm in the UV, and at $\lambda \approx 3$ μm. However, signal propagation
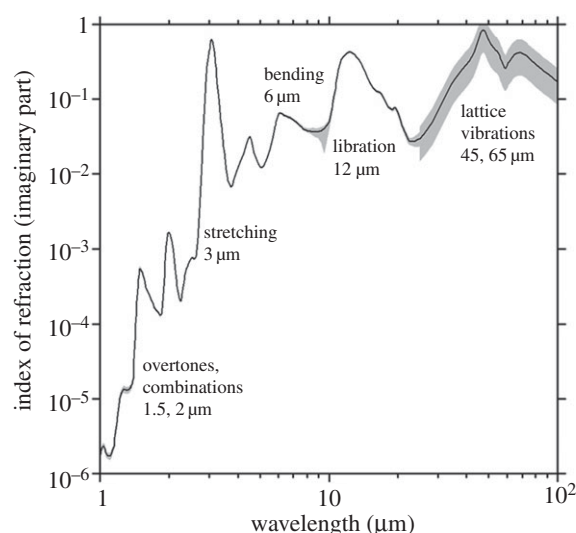
Figure 2. Expansion of figure 1*e*, annotated. Shading indicates uncertainty. The 1.5 μm peak may be inaccurate, based on evidence from snow spectral albedo measurements [6].

does not exceed the free-space speed of light, c. This topic is discussed by Bohren & Huffman ([5], §9.1.3).

At the UV absorption edge at $\lambda \approx 180$ nm, m_{im} drops by a factor 10^{10}, and it is below the detection limit of available experiments in the near-UV, 200–400 nm. The IR absorptions (1–100 μm) can be assigned as indicated in figure 2 (an expansion of figure 1*e*). The fundamental vibrational modes of the water molecule are seen in ice: bending at 6 μm, and both symmetric and asymmetric stretch overlapping at 3 μm. The weaker bands at 1.5 and 2 μm have not been identified in detail; they include overlapping overtones and combinations of the fundamental modes.

These vibrational modes, because they are intramolecular, are also seen in water vapour, shifted somewhat in frequency by the formation of the hydrogen bond in ice. The stretching modes for the vapour (ν_1 and ν_3) are shifted to lower frequency by 16% in ice (table 2.1 of [7]), indicating that formation of the hydrogen bond between two molecules weakens the spring constant for stretching of the covalent O–H bond. By contrast, the bending mode (ν_2) is shifted to *higher* frequency by 3% in ice, indicating a stiffening of the spring constant for bending, as formation of the hydrogen bonds requires the H–O–H angle to open from its equilibrium value for the isolated molecule (104.5°) towards the tetrahedral angle of the ice crystal (109.5°).

The water-vapour rotation band at $\lambda > 20$ μm is shifted to shorter wavelength in ice as the libration (hindered rotation) band at 12 μm. Lattice vibrations appear at 45 and 65 μm; they have no counterpart in the vapour because they are intermolecular vibrations of the hydrogen bond.

Comparing figure 1*b* to figure 1*e* shows the relationship of m_{re} to m_{im}: wherever m_{im} is large (of order 1), the real index undergoes an oscillation, finally asymptoting to a higher level at longer wavelength, increasing from 1.3 in the visible to 1.8 in the microwave. The real and imaginary indices are related by Kramers–Kronig relations; in fact the $m_{re}(\lambda)$ in figure 1 was computed from a weighted integral of m_{im} over wavelength as detailed by Warren [3] and WB08 [4].

(b) Birefringence

Ordinary ice has a hexagonal crystal structure, so it is birefringent; refraction depends on the angle between the *c*-axis of the crystal and the direction and polarization of the incident light. For example, at the visible wavelength 546 nm, $m_{re} = 1.3104$ for the ordinary ray and 1.3118

for the extraordinary ray ([8], table 3.1). This small difference, only 0.1%, can be ignored for computing reflectances and transmittances of clouds and snow, but it is large enough to be useful for determining crystal sizes and orientations in polycrystalline ice by putting a thin section of ice between crossed polarizers. This method is routinely used for crystal-fabric studies of glacier ice (e.g. [9]).

## (c) Visible and near-ultraviolet absorption

Water has no absorption mechanism centred in the visible or near-UV, 200–700 nm. The observed absorption by water and ice in this region is the tail of near-IR vibrational absorptions, decreasing with decreasing wavelength to extremely small values before finally increasing at the first UV absorption at approximately 180 nm.

Across the visible spectrum the absorption decreases with decreasing wavelength from red to blue, becoming so weak that Grenfell & Perovich ([1]; hereafter GP) needed a 3 m long block of ice to obtain significant measurable attenuation. They devised a method to grow bubble-free ice in the laboratory, obtaining the minimum attenuation at $\lambda = 470$ nm. Their measurement was of transmission, which is reduced not only by absorption but also by scattering. Although their ice was bubble-free and appeared visually clear, there was still a small amount of Rayleigh scattering due to crystal defects or density fluctuations in the ice. This scattering became the dominant source of attenuation at the blue end of the spectrum, as was pointed out by Price & Bergström [10]. Price & Bergström showed that reported 'absorption' coefficients for several transparent minerals increased from the visible into the near-UV, following closely a λ^{-4} dependence indicative of Rayleigh scattering: not only ice but also LiF, $BaTiO_3$ and diamond. Price & Bergström concluded that in all those measurements scattering had been misinterpreted as absorption.

A different kind of experiment was therefore needed. In measurements made to test the Antarctic Muon and Neutrino Detector Array (AMANDA), coefficients for both absorption and scattering were inferred for glacier ice 800–1800 m deep in the Antarctic Ice Sheet. What was measured was the distribution of photon arrival times at an array of detectors in a borehole, the photons originating from a pulsed source in another borehole some distance away. At those depths, the scattering coefficient is small because most of the air bubbles have dissolved in the ice as clathrates, but the ice does contain natural fallout of dust (e.g. as nuclei for snow-crystal formation) which contributes to the absorption. The distribution of photon arrival times was fitted to a function with two coefficients, a scattering coefficient and an absorption coefficient [11]. The resulting absorption coefficient at $\lambda = 400$ nm was about a factor of 20 smaller than that reported by GP [1]. Even so, AMANDA's k_a is an upper limit because of the absorption by dust in the ice.

AMANDA's low values of k_a were confirmed by measurements of spectral transmission of sunlight into Antarctic surface snow ([12]; hereafter WBG). As summarized by WB08 [4], snow is a scattering-dominated medium whose scattering coefficient is independent of wavelength across the visible and near-UV. The attenuation of solar radiation in snow can be used to infer k_a by reference to the known value at $\lambda = 600$ nm (where GP [1] and AMANDA were in agreement). WBG [12] developed this method and derived values of k_a for wavelengths 350–600 nm from measurements at Dome C on the East Antarctic Plateau. The minimum absorption was found at $\lambda_{min} = 390$ nm in agreement with AMANDA, in contrast to $\lambda_{min} = 470$ nm reported by GP [1] and used by Warren [3]. The value of k_a at 390 nm inferred by WBG [12] is lower than even the lowest values of AMANDA, by a factor of 6. A subsequent more extensive set of similar measurements in snow by Picard *et al.* [13] at the same location found values of k_a intermediate between the two AMANDA measurements.

The blue and near-UV absorption by ice is so weak, with photon mean free paths before absorption of hundreds of metres in pure ice, that k_a is essentially zero for some purposes, for example, in computing albedo and transmittance of clouds. The non-zero values of k_a have a slight effect on snow albedo, less than 1%. The exact value of k_a does matter for computation of
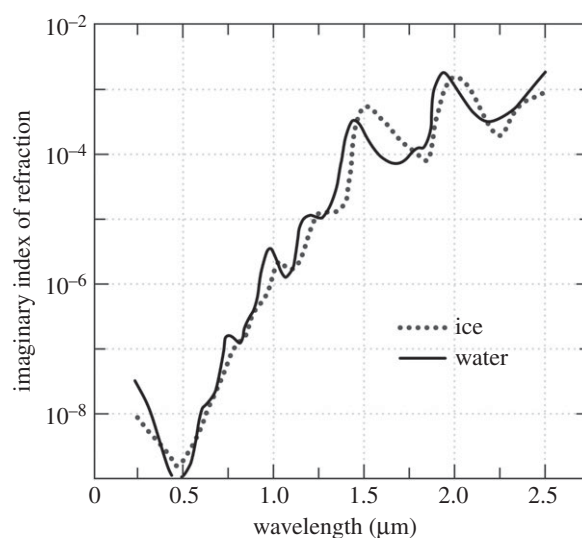
Figure 3. Comparison of the absorption spectra of ice and water in the visible and near-IR region, shown as the imaginary part of the complex index of refraction. From fig. 1 of Dozier [24], modified and redrawn. The ice spectrum for $\lambda < 0.5\,\mu$m shown here is now superseded by the plot in figure 1*d*.

photochemical fluxes in snow (e.g. [14]) and of ice thickness on the tropical ocean of 'Snowball Earth' [15].

(d) Temperature dependence, cubic ice, amorphous ice, liquid water

For ice Ih, the temperature dependence of k_a is small for UV, visible and near-IR wavelengths. It is significant in the mid-IR and far-IR bands, where measurements have been made for temperatures between the cubic–hexagonal transition and the melting point [16,17], as reviewed by WB08 [4]. The lattice vibrations shift to longer wavelength at higher temperature. Woschnagg & Price [18] reviewed several experimental studies, concluding that k_a increases with temperature by approximately 1% K^{-1} for all weakly absorbing parts of the spectrum from the UV to the microwave. Beyond 1 cm wavelength, absorption increases more rapidly with temperature; a convenient equation is given by Mätzler [19].

In both hexagonal and cubic ice (Ih and Ic), each water molecule is hydrogen-bonded to four tetrahedrally arranged neighbours; it is only in the second-nearest neighbours that their structures differ. Correspondingly, the absorption spectrum of cubic ice is close to that of hexagonal ice in the few spectral regions where it has been measured [20], except for the systematic temperature dependence. Amorphous ice is different, especially in the far-IR. Absorption spectra in the mid-IR region were reported for both cubic and amorphous ice by Mastrapa *et al*. [21].

The spectrum of liquid water is close to that of ice from the UV to the near-IR, but they diverge in the thermal IR and become very different in the far-IR, microwave and radio-wave regions [22]. The reported absorption length k_a^{-1} for liquid water reaches a maximum of approximately 250 m at $\lambda = 420$ nm [23]. Although the visible and near-IR absorption spectra of ice and water are very similar, they are shifted in wavelength in some regions sufficiently to be useful for remote sensing, for example, to identify the phase of clouds by reflectance at $\lambda = 1.6\,\mu$m (figure 3) and to detect liquid water in snow [25].

A notable characteristic of the spectra shown in figures 1–3 is that the spectra are smooth; an accurate tabulation can be accomplished with coarse spectral resolution, in contrast to the line structure of gases. These smooth spectra are typical of condensed phases (liquid and solid). Figure 4 is a textbook example of the contrast, using CH_3I for illustration. The spectra of liquid
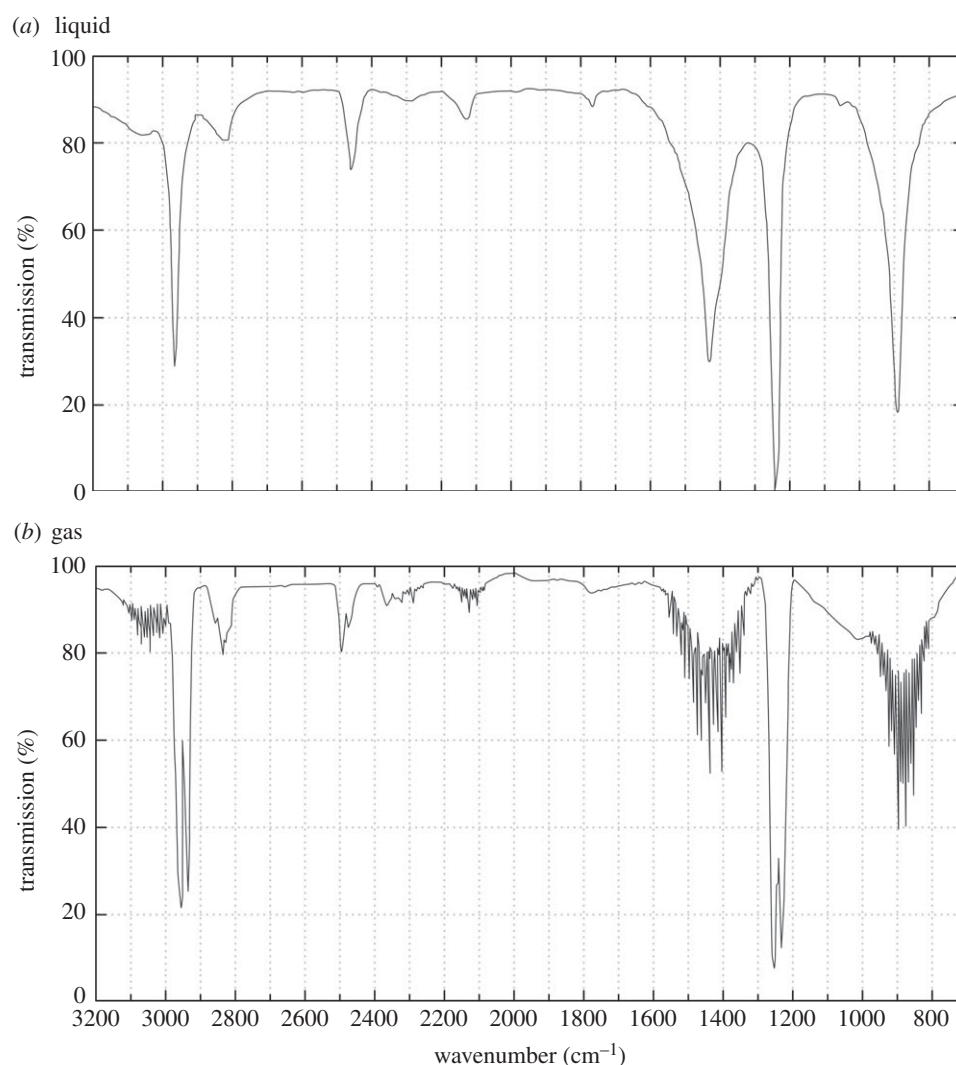
Figure 4. Infrared transmission spectrum of methyl iodide (CH₃I) (*a*) as a liquid and (*b*) as a vapour. From fig. 7-1 of Barrow [26], modified and redrawn.

and vapour are qualitatively similar, but the lines of the vapour spectrum (corresponding to different rotational states) merge into a single broad absorption feature in the liquid. One way to think of this is that, in the liquid, the molecules experience a high frequency of collisions, resulting in extreme collision broadening of the lines.

3. Optical properties in the solar spectrum

By 'optical properties' (as opposed to optical constants) we normally mean the absorptance, transmittance, reflectance (albedo) and emissivity of bulk media such as snow, sea ice and clouds, expressed as ratios from 0.0 to 1.0. For example, the albedo is the upward (reflected) flux divided by the downward (incident) flux of solar energy onto a surface.

The interaction of radiation with matter depends on the spatial scales of inhomogeneity relative to the wavelength of light. Radiation interacts with matter over a distance comparable to the wavelength; the electromagnetic wave is not affected by irregularities on scales much smaller than the wavelength. For example, pure bubble-free ice looks homogeneous to visible light but

not to X-rays. At $\lambda \approx 0.1$ nm (X-ray), the wave diffracts off the oxygen–oxygen bond distance (0.28 nm). Moving up seven orders of magnitude to $\lambda \approx 1\,\mu$m (near-IR), the wave sees a sharp discontinuity at each air–ice interface, so in snow the relevant physical processes are reflection off, and refraction through, snow grains of size $\gg 1\,\mu$m. Moving up another six orders of magnitude to $\lambda \sim 1$ m, a radio wave emitted downwards from an airborne radar source to the snow-covered surface of an ice sheet does not see a discontinuity at every grain, but does see a discontinuity at the top surface, a discontinuity not between air and ice but between air and *snow*. The snow reflects like a mirror, with an average refractive index (or dielectric constant) determined by the snow density.

(a) Snow

Snow is a mixture of air and ice. Solar photons re-emerge from snow not just by reflection at the surface but more importantly by successive refraction through subsurface snow grains. Photons have an opportunity to change direction at each air–ice interface, and they have a chance of being absorbed as they pass through ice. Many natural snowpacks, especially snowpacks of cold fine-grained snow, are thick enough that little light is transmitted through to the underlying surface, so in that case the absorptance and reflectance together add to 1.0. (Coarse-grained snow is more transmissive, as shown in figure 5a.) At any particular wavelength, the most important variable is the snow grain size r [28]. In the solar spectrum, where $r \gg \lambda$, it is common to model a non-spherical snow particle as a collection of independent spheres, such that the collection of spheres has the same total area and same total mass as the non-spherical particle [29]. The radius of the spheres r_e in the model snowpack is then three times the volume-to-area ratio of the real non-spherical snowpack. It is also reciprocally related to the area-to-mass ratio, the 'specific surface area' SSA [30], as

$$\text{SSA} = \frac{3}{r_e \rho_{\text{ice}}}, \qquad (3.1)$$

where ρ_{ice} is the density of pure ice, $917\,\text{kg}\,\text{m}^{-3}$. The errors in this spherical representation have been quantified for various snow-crystal shapes [31–33]. The extinction efficiency and single-scattering albedo are well represented by the equivalent spheres. The scattering asymmetry factor for the spheres is too large, but its effect on bulk optical properties can be compensated by reducing the model's grain size [34]. The equivalent-sphere representation is appropriate only where $r \gg \lambda$, so it fails in the microwave region, where snow density becomes an important variable.

In coarse-grained snow, a photon travels a longer distance through ice between opportunities for scattering than in fine-grained snow, so it is more likely to be absorbed, and therefore a snowpack of coarse grains has lower albedo. The area-to-mass ratio normally decreases with snow age by 'destructive metamorphism' [35], so the radiatively effective grain size r_e increases, and the albedo drops. Figure 5a shows the computed spectral albedo for various thicknesses of snow with $r_e = 1$ mm (a grain size typical of old melting snow).

The theory of the optics of snow is treated in detail by Kokhanovsky & Zege [36].

(i) Wet snow

Even slight melting causes a rapid increase of grain size, so that wet snow has lower albedo than dry snow in the near-IR. When wet snow was refrozen in a laboratory experiment, O'Brien & Munis ([37], their fig. 6) found essentially no change in the spectral albedo; it remained low. In discussing this experiment, Wiscombe & Warren [28] noted that the refractive index of water (1.33) is close to that of ice (1.31), so that: 'the replacement of air by liquid water between ice grains can increase the effective grain size. There was no further change in albedo when the sample was refrozen. There was then no liquid water present, but the water bridges between grains had presumably frozen, with no change in the effective grain size.' O'Brien & Munis's fig. 6 was reproduced as fig. 10 of Wiscombe & Warren [28] and fig. 5 of Warren [29].

(a)

(b)
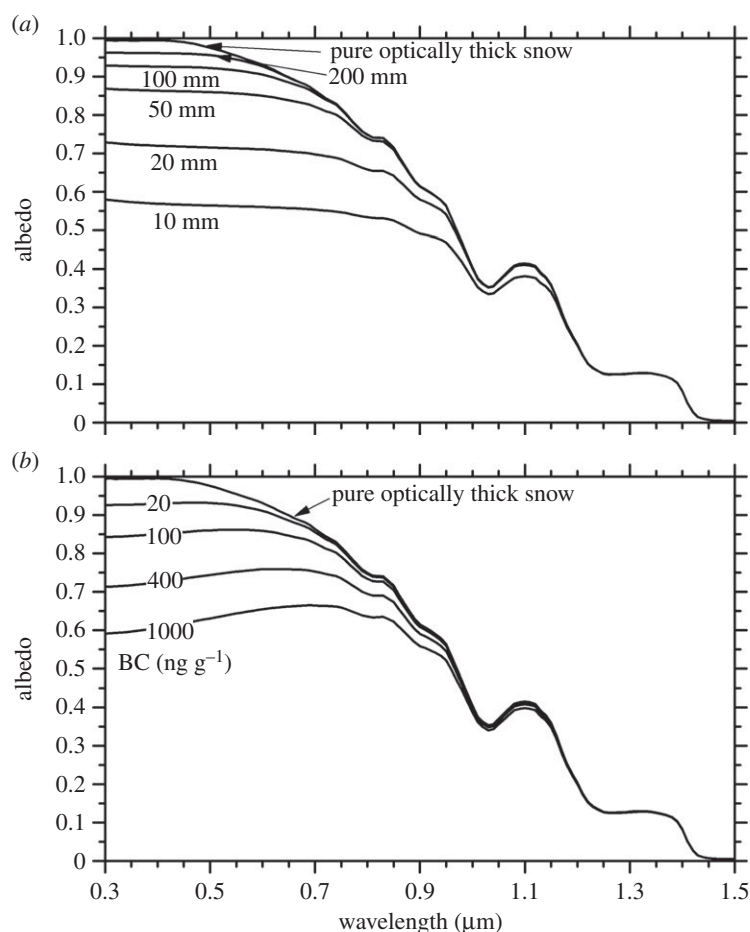
Figure 5. Comparison of the spectral signature of snow thinness to that of black carbon (BC) in snow, for snow grain radius $r_e = 1$ mm and solar zenith angle 60°. (*a*) Spectral albedo of pure snow over a black surface for a variety of snow depths expressed in liquid equivalent. The top curve is for semi-infinite depth. (*b*) Spectral albedo of deep snow containing various mixing ratios of BC in parts per billion by mass (nanograms of BC per gram of snow). (Figure and caption from fig. 1 of Warren [27].)

Wet snow can be identified in remote sensing using narrow spectral channels at 940 and 1050 nm [25], making use of the offsetting of absorption peaks and valleys for water and ice in this spectral region (figure 3).

(b) Lake ice and sea ice

The surface waters of lakes and oceans are normally saturated with dissolved air. Oxygen and nitrogen molecules cannot be incorporated into the ice crystal lattice, so when the water freezes the dissolved air comes out of solution as bubbles, which become trapped between crystals in the growing ice. These bubbles, as well as cracks caused by thermal contraction, are responsible for the scattering of sunlight by lake ice [39].

Seawater additionally contains dissolved salt, which likewise cannot be incorporated into the ice lattice. But because the downward growth of sea ice exhibits fingering due to 'constitutional supercooling' [40], pockets of brine become enclosed in the growing ice, and the bulk salinity of newly formed sea ice is about one-third that of seawater. The refractive-index contrast of an ice–brine interface [41] is smaller than that of an ice–air interface, but in first-year ice below
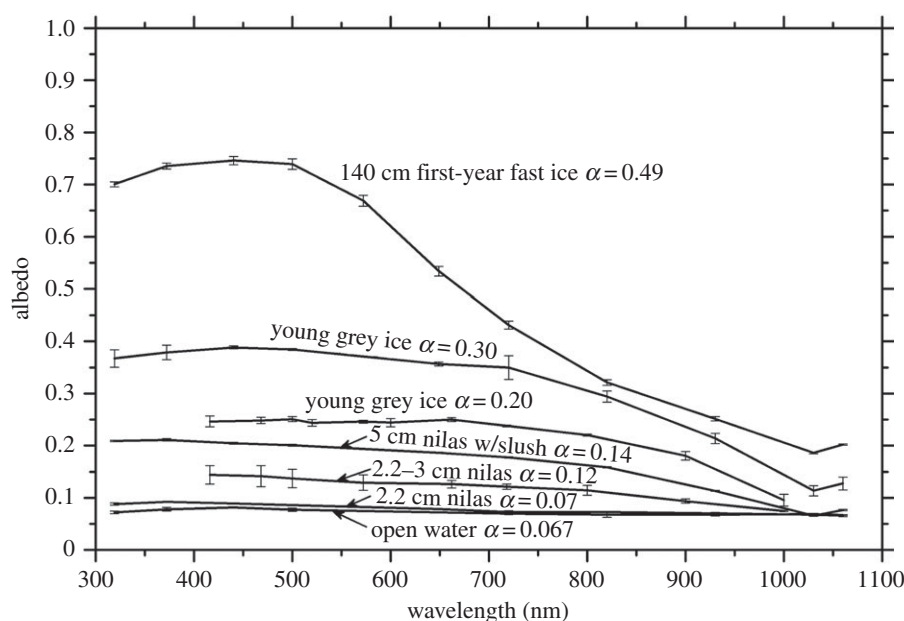
Figure 6. Spectral albedos of snow-free sea ice, and open water. Broadband solar albedo α is also given. Ice thickness is given, except for two ice types that were observed only from a helicopter. From fig. 1 of Brandt *et al*. [38].

freeboard the total cross-sectional area of brine inclusions greatly exceeds that of the air bubbles [42], so brine can be more important than air in determining the scattering properties of sea ice. In drained multi-year ice the area of air–ice interfaces is greater, so they dominate the scattering [43]. The spectral albedo of bare (snow-free) sea ice of different thicknesses is shown in figure 6.

(c) Marine ice

Ice crystals form in supercooled seawater beneath several Antarctic ice shelves; as they float up to the ice-shelf base they scavenge particles from the water and incorporate them into the growing basal ice. The resulting 'marine ice' can be approximately 100 m thick [44]; it differs from sea ice in that it is clear, desalinated and bubble-free. Icebergs calving from the front of these ice shelves are therefore composite icebergs; the upper part is glacial ice originating from snow, and the lower part is marine ice. This marine ice is hidden below the water-line, but if the iceberg's horizontal extent is small enough it may capsize, exposing the marine ice. Icebergs of marine ice vary in colour from blue to green, depending on the nature and abundance of foreign constituents in the seawater that became trapped in the ice as it grew. The addition of dissolved organic matter (gelbstoff) or iron oxides to ice can shift the colour of marine ice from blue to green [45,46].

(d) The transition snow–firn–glacier ice

On the surface of an ice sheet, snow (with density typically 300–400 kg m^{-3}) is compressed under its own weight into *firn* (density 550–830 kg m^{-3}). With further compression, the air becomes closed off into bubbles when the density reaches approximately 830 kg m^{-3}, and the material is then called glacier ice. Deeper in the ice sheet, the bubbles become smaller under pressure and eventually dissolve in the ice as a clathrate.

Bare glacier ice is exposed in areas near the Trans-Antarctic Mountains called 'blue-ice areas', where strong winds blow the snow away and sublimate ice at a rate of approximately 5 cm per year [47]. There is an upward flow of glacier ice to replace the loss by sublimation. In places
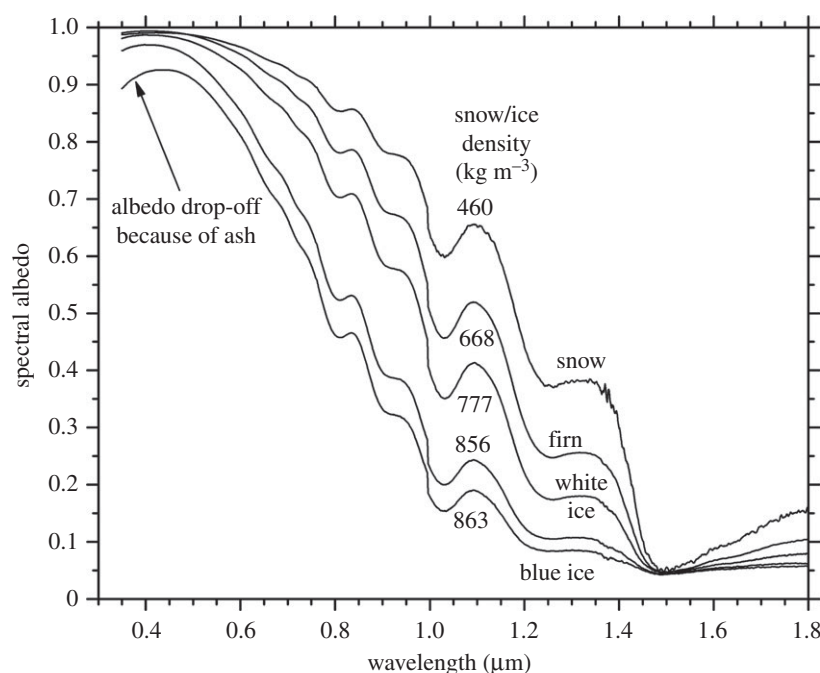
Figure 7. Spectral albedos of surface types on a 6 km transect from the accumulation zone into the ablation zone of the Allan Hills blue-ice region in the Trans-Antarctic Mountains. The density of the top 10 cm is indicated. Modified from fig. 6 of Dadic et al. [50].

the ice at the surface is 2–3 million years old [48,49]. As the upward-flowing ice approaches the surface and becomes depressurized, the bubbles re-form from clathrate. Upstream of these areas a transect of a few kilometres exposes a sequence of surface types: snow, firn, young white ice, old blue ice. In this sequence, the albedo decreases systematically at all wavelengths as the density increases (figure 7). The albedos are explained by radiative transfer modelling; the specific surface areas required to match the observations were larger than were found by X-ray tomography of core samples [50]. The most likely explanation for the discrepancy is that the models used the scattering pattern for spherical bubbles, but the real non-spherical bubbles have smaller scattering asymmetry factors [34,50].

4. Ice is blue but snow is white

Ice is a weak filter for red light. As shown in figure 1, the absorption coefficient of ice increases with wavelength from blue to red. The absorption length, k_a^{-1}, is approximately 2 m at $\lambda = 700$ nm but approximately 200 m at $\lambda = 400$ nm. Photons at all wavelengths of visible light will survive without absorption, and be reflected or transmitted, unless the path length through ice is long enough to significantly absorb the red light. In snow the grain radii are typically approximately 100 µm, so even if 1000 refraction events are needed for a photon to re-emerge at the surface, it will have passed through only 20 cm of ice. Snow is therefore white; the albedo of Antarctic surface snow decreases only slightly from 0.99 at 400 nm to 0.96 at 700 nm (fig. 6 of [51]). Ice develops a noticeable blue colour in glacier crevasses and in icebergs, especially in marine ice because of its lack of bubbles (see photographs in [52]).

The snow surface on the interior plateau of Antarctica has a stable albedo because it is continually renewed by light snowfall throughout the summer. Because of this stability, the Antarctic Plateau has been used as a calibration target to monitor the drift in sensitivity of visible channels on satellites [53,54].
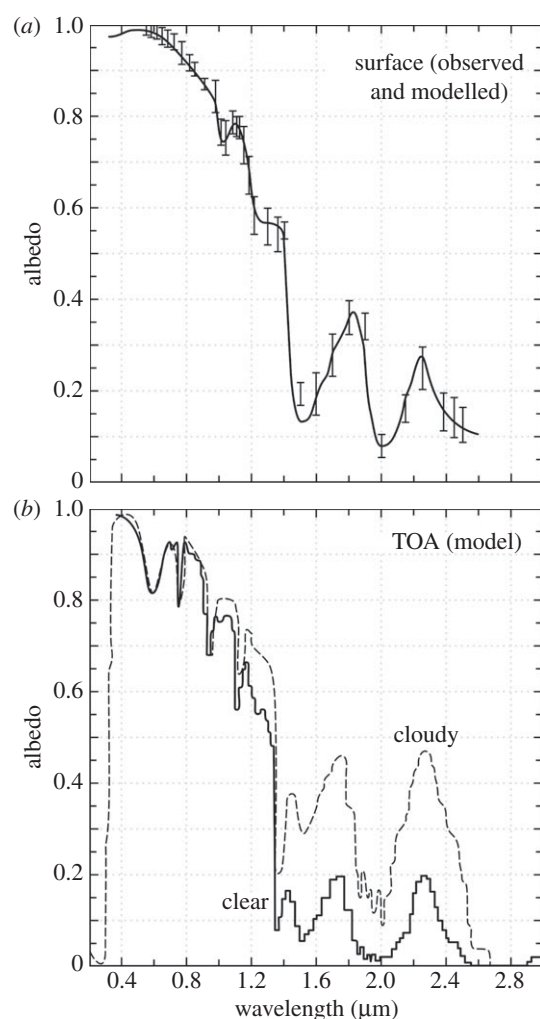
Figure 8. (*a*) Measured (with error bars) and modelled spectral albedo of Antarctic snow, from Grenfell *et al*. [55]. (*b*) Spectral albedo at the top of the atmosphere (TOA), from radiative-transfer model calculations, over Plateau Station (79° S) with solar zenith angle 66° for a clear sky (solid line) and with a cirrostratus cloud at 1.0–2.7 km height (3.7 particles cm^{-3}, effective radius = 15.6 μm, dashed line). The near-IR albedo is higher when the cloud is present, but the visible albedo is unchanged. The dip in TOA albedo at wavelength 0.6 μm is due to absorption by ozone. The drop-off of TOA albedo at $\lambda < 0.3$ μm is due to the strong UV absorption by ozone. From fig. 1 of Masonis & Warren [54], modified and redrawn.

5. Clouds over snow

If we look down from the top of the atmosphere (e.g. from a satellite) at the snow surface of an ice sheet, should its appearance change if an ice cloud is added to the scene? All that has happened is that a thin layer of ice crystals was inserted over an already thick layer of ice crystals.

Perhaps surprisingly, the cloud does indeed change the appearance of the scene, in two ways. First, the particle sizes are smaller in the cloud than in the snow (typical effective radii r_e of 10 μm versus 100 μm), so the albedo of the cloud scene is higher at wavelengths that are sensitive to r_e, namely the near-IR, especially at 1.7 and 2.2 μm wavelength (figure 8). The 1.7 μm region is used to distinguish snow from clouds in satellite remote sensing.

Secondly, there is an effect on the visual appearance. The visible albedo of the scene is not affected by the cloud, but the angular distribution of reflected radiation is altered. Snow surfaces are rough on scales large compared to the few-centimetre penetration depth of visible light, particularly by the wind-erosion features called sastrugi [56]. When the Sun is low, a flat snow surface scatters light primarily into the forward direction. A rough surface reduces the forward scattering and sends more reflected light upwards, into near-vertical directions [51,57,58]. Covering the rough snow with a cloud, whose roughness length (in units of optical depth) is smaller than that of snow, restores the forward scattering pattern, darkening the nadir view [59].

## 6. Light-absorbing impurities in snow

The absorption coefficient of ice is so small at visible and near-UV wavelengths that parts-per-billion (ppb) amounts of absorptive impurities can dominate the absorption and significantly reduce the snow albedo [60–62]. The important impurities are black carbon (soot), brown (organic) carbon and mineral dust. The main absorbers in mineral dust are iron oxides [63,64]. Figure 5*b* shows the effect of adding black carbon (BC) to coarse-grained snow. The albedo is reduced at visible and near-UV wavelengths, but not in the near-IR for $\lambda > 1\,\mu m$, where ice itself is moderately absorptive so that trace amounts of BC have little effect.

Light-absorbing impurities in snow have been surveyed on field expeditions in the Arctic [65,66], North America [67] and China [68,69]. Some measurements were also made on the Antarctic Plateau [12,55,70] and on Antarctic sea ice [71]. The values of BC range over four orders of magnitude, from 0.2 ppb in the Antarctic and 2 ppb on Greenland, to 2000 ppb in remote areas of northeast China. The Arctic snow outside of Greenland has typically 20 ppb of BC, which is sufficient to reduce snow albedo by approximately 1%, depending on snow grain size. This small change in albedo is difficult to detect by radiation measurements at the surface, and even more difficult to detect by remote sensing [27], but it is important for climate. For the incident solar energy of $400\,W\,m^{-2}$ typical of late spring and early summer in the Arctic, a 1% reduction of albedo causes a diurnal average radiative forcing of $4\,W\,m^{-2}$ locally, similar to that of doubling CO_2.

7. Infrared emissivity of snow

In contrast to the solar wavelengths (near-UV, visible and near-IR), where snow albedo varies dramatically with wavelength and is sensitive to snow grain size and snow depth, the radiative properties of snow at thermal IR wavelengths are much less variable. The emissivity of snow is independent of snow depth and impurities. It is very high for fine-grained snow, 0.98–0.99 across the infrared 'window' from 8 to 13 μm wavelength [72]. The emissivity of coarse-grained snow becomes sensitive to viewing angle; it is as low as 0.93 for a viewing zenith angle of 75° at $\lambda = 13\,\mu m$.

Two attempts to model the spectral emissivity [73,74] obtained opposite dependences on grain size. The measurements of Hori *et al.* [72] agreed with the prediction of Wald [74] in finding the emissivity to decrease with increasing grain size. The Dozier–Warren model [73] had used Mie theory [75] for single scattering, which assumes that the scattering properties of a snow grain are not affected by the proximity of neighbouring grains. That approach worked well in the solar spectrum, where the sizes of the snow grains, and the air spaces between snow grains, are large compared to the wavelength. For the thermal infrared Dozier & Warren [73] considered the medium surrounding a snow grain to be a mixture of air and ice, to make a correction for close packing, dependent on snow density. Wald's method [74] added a specular component which lowered the emissivity for coarse-grained snow, in better agreement with the measurements of Hori *et al.* [72]. Wald's modelling approach was modified by Hori *et al.* [76] to include an empirical parameter to better fit the experimental data.
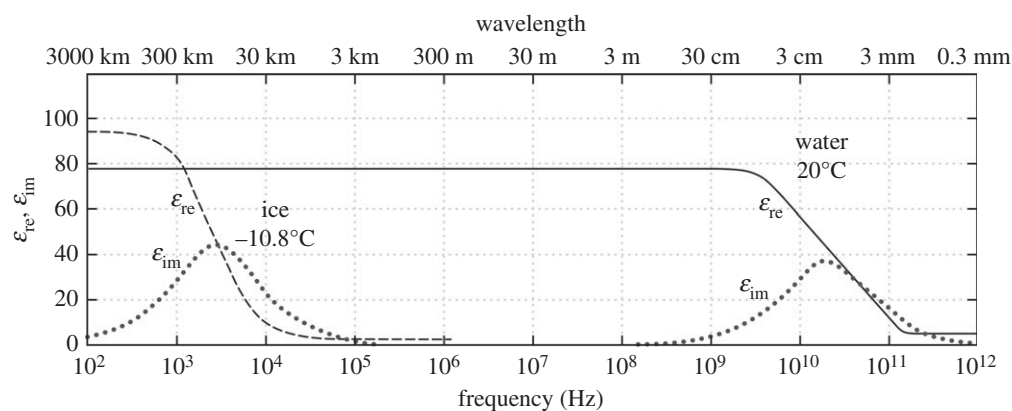
Figure 9. The dielectric behaviour of ice and water as functions of frequency. The symbols ε_{re} and ε_{im} are the real and imaginary parts of the complex relative permittivity, respectively. The complex relative permittivity is the square of the complex index of refraction. From fig. 3 of Hoekstra & Cappillino [83].

8. Remote sensing of snow and ice

Remote sensing of the cryosphere is a large research field, which I will not attempt to review. Instead, I refer the reader to two books [77,78] and two review articles [79,80]. I will just briefly comment here on remote sensing using microwaves and radio waves.

In the microwave region, ice and water differ greatly in their absorption coefficients, so the fractional coverage of sea ice can be determined from microwave brightness temperatures (e.g. [81]). For example, at $\lambda = 1.55$ cm (frequency 19 GHz), the vertical emissivity of water is 0.43, but for ice it is 0.92. Sea ice is routinely mapped by passive microwave observations from satellite, making use of this emissivity contrast. The signal received by the satellite is unaffected by clouds because cloud particles are much smaller than the 1.55 cm wavelength. Again, because of this difference in microwave absorption between ice and water, melting of surface snow can be detected on the ice sheets of Greenland and Antarctica, allowing for monitoring of the melt extent in summer (e.g. [82]).

Continuing to longer wavelength, where the absorption mechanism is 'dielectric relaxation', the medium becomes most absorptive when the dielectric response is approximately 90° out of phase with the oscillating electric field. This absorption for ice peaks at 3×10^3 Hz; for water at 2×10^{10} Hz (figure 9). Between these absorption features there is a long region of wavelengths, 1–100 m, where neither water nor ice is absorptive. The wavelength range 3–10 m is used for radio-echo sounding of ice sheets because these wavelengths can penetrate several kilometres of ice-sheet depth [84].

9. Suggestions for future research

Here are just a few ideas for research projects.

(1) Develop new methods to quantify the extremely small absorption coefficient of ice in the UV–blue spectral region.

(2) Confirm with measurements the modelled quantitative relation between impurity content and reduction of snow albedo. Some attempts have been made [85,86], but more are needed, with different sizes of impurity particles and snow grains.

(3) Determine the microlocation of BC particles in snow. Particles located in the interior of snow grains are more effective at albedo reduction than if they are on the grain surfaces [87].

(4) Biological processes are important for the radiation budget on glaciers and ice sheets in locations and seasons where melting is occurring. Characterization of the red algae in snow and black algae in ice could be crucial to understanding melt rates on Greenland [88,89].

References

1. Grenfell TC, Perovich DK. 1981 Radiation absorption coefficients of polycrystalline ice from 400 to 1400 nm. *J. Geophys. Res.* **86**, 7447–7450. (doi:10.1029/JC086iC08p07447)
2. Schaaf JW, Williams D. 1973 Optical constants of ice in the infrared. *J. Opt. Soc. Am.* **63**, 726–732. (doi:10.1364/JOSA.63.000726)
3. Warren SG. 1984 Optical constants of ice from the ultraviolet to the microwave. *Appl. Opt.* **23**, 1206–1225. (doi:10.1364/AO.23.001206)
4. Warren SG, Brandt RE. 2008 Optical constants of ice from the ultraviolet to the microwave: a revised compilation. *J. Geophys. Res.* **113**, D14220. (doi:10.1029/2007JD009744)
5. Bohren CF, Huffman DR. 2004 *Absorption and scattering of light by small particles*. Wiley Professional Paperback Edition. Weinheim, Germany: Wiley-VCH. (doi:10.1002/9783527618156)
6. Carmagnola CM *et al.* 2013 Snow spectral albedo at Summit, Greenland: measurements and numerical simulations based on physical and chemical properties of the snowpack. *Cryosphere* **7**, 1139–1160. (doi:10.5194/tc-7-1139-2013)
7. Fletcher NH. 1970 *The chemical physics of ice*. Cambridge, UK: Cambridge University Press.
8. Hobbs PV. 1974 *Ice physics*. Oxford, UK: Clarendon Press.
9. Gow AJ, Meese D. 2007 Physical properties, crystalline textures, and *c*-axis fabrics of the Siple Dome (Antarctica) ice core. *J. Glaciol.* **53**, 573–584. (doi:10.3189/002214307784409252)
10. Price PB, Bergström L. 1997 Optical properties of deep ice at the South Pole: scattering. *Appl. Opt.* **36**, 4181–4194. (doi:10.1364/AO.36.004181)
11. Ackermann M *et al.* 2006 Optical properties of deep glacial ice at the South Pole. *J. Geophys. Res.* **111**, D13203. (doi:10.1029/2005JD006687)
12. Warren SG, Brandt RE, Grenfell TC. 2006 Visible and near-ultraviolet absorption spectrum of ice from transmission of solar radiation into snow. *Appl. Opt.* **45**, 5320–5334. (doi:10.1364/AO.45.005320)
13. Picard G, Libois Q, Arnaud L. 2016 Refinement of the ice absorption spectrum in the visible using radiance profile measurements in Antarctic snow. *Cryosphere* **10**, 2655–2672. (doi:10.5194/tc-10-2655-2016)
14. Wolff EW, Jones AE, Martin TJ, Grenfell TC. 2002 Modelling photochemical NO_x production and nitrate loss in the upper snowpack of Antarctica. *Geophys. Res. Lett.* **29**, 1944. (doi:10.1029/2002GL015823)
15. Warren SG, Brandt RE, Grenfell TC, McKay CP. 2002 Snowball Earth: ice thickness on the tropical ocean. *J. Geophys. Res.* (*Oceans*) **107**, 3167. (doi:10.1029/2001JC001123)
16. Toon OB, Tolbert MA, Koehler BG, Middlebrook AM, Jordan J. 1994 Infrared optical constants of H_2O ice, amorphous nitric acid solutions, and nitric acid hydrates. *J. Geophys. Res.* **99**, 25 631–25 654. (doi:10.1029/94JD02388)
17. Curtis DB, Rajaram B, Toon OB, Tolbert MA. 2005 Measurement of the temperature-dependent optical constants of water ice in the 15–200 μm range. *Appl. Opt.* **44**, 4102–4118. (doi:10.1364/AO.44.004102)
18. Woschnagg K, Price PB. 2001 Temperature dependence of absorption in ice at 532 nm. *Appl. Opt.* **40**, 2496–2500. (doi:10.1364/AO.40.002496)

19. Mätzler C. 2006 Microwave dielectric properties of ice. In *Thermal microwave radiation: applications for remote sensing* (eds C Mätzler, PW Rosenkranz, A Battaglia, JP Wigneron). IET Electromagnetic Waves Series 52, chapter 5.3, pp. 455–462. Stevenage, UK: Institute of Engineering and Technology.

20. Bertie JE, Whalley E. 1967 Optical spectra of orientationally disordered crystals. II. Infrared spectrum of ice Ih and ice Ic from 360 to $50 \, \text{cm}^{-1}$. *J. Chem. Phys.* **46**, 1271–1284. (doi:10.1063/1.1840845)

21. Mastrapa RM, Sandford SA, Roush TL, Cruikshank DP, Dalle Ore CM. 2009 Optical constants of amorphous and crystalline H_2O-ice: 2.5–22 μm (4000–455 cm^{-1}). *Astrophys. J.* **701**, 1347–1356. (doi:10.1088/0004-637X/701/2/1347)

22. Irvine WM, Pollack JB. 1968 Infrared optical properties of water and ice spheres. *Icarus* **8**, 324–360. (doi:10.1016/0019-1035(68)90083-3)

23. Pope RM, Fry ES. 1997 Absorption spectrum (380–700 nm) of pure water. II. Integrating cavity measurements. *Appl. Opt.* **36**, 8710–8723. (doi:10.1364/AO.36.008710)

24. Dozier J. 1989 Estimation of properties of alpine snow from Landsat Thematic Mapper. *Adv. Space Res.* **9**, 207–215. (doi:10.1016/0273-1177(89)90487-0)

25. Green RO, Painter TH, Roberts DA, Dozier J. 2006 Measuring the expressed abundance of the three phases of water with an imaging spectrometer over melting snow. *Water Resour. Res.* **42**, W10402. (doi:10.1029/2005WR004509)

26. Barrow GM. 1962 *Introduction to molecular spectroscopy*. New York, NY: McGraw-Hill.

27. Warren SG. 2013 Can black carbon in snow be detected by remote sensing? *J. Geophys. Res.* **118**, 779–786. (doi:10.1029/2012JD018476)

28. Wiscombe WJ, Warren SG. 1980 A model for the spectral albedo of snow. I: Pure snow. *J. Atmos. Sci.* **37**, 2712–2733. (doi:10.1175/1520-0469(1980)037<2712:AMFTSA>2.0.CO;2)

29. Warren SG. 1982 Optical properties of snow. *Rev. Geophys. Space Phys.* **20**, 67–89. (doi:10.1029/RG020i001p00067)

30. Matzl M, Schneebeli M. 2006 Measuring specific surface area of snow by near-infrared photography. *J. Glaciol.* **52**, 558–564. (doi:10.3189/172756506781828412)

31. Grenfell TC, Warren SG. 1999 Representation of a nonspherical ice particle by a collection of independent spheres for scattering and absorption of radiation. *J. Geophys. Res.* **104**, 31 697–31 709. (doi:10.1029/1999JD900496)

32. Neshyba SP, Grenfell TC, Warren SG. 2003 Representation of a nonspherical ice particle by a collection of independent spheres for scattering and absorption of radiation. II. Hexagonal columns and plates. *J. Geophys. Res.* **108**(D15), 4448. (doi:10.1029/2002JD003302)

33. Grenfell TC, Neshyba SP, Warren SG. 2005 Representation of a nonspherical ice particle by a collection of independent spheres for scattering and absorption of radiation. 3. Hollow columns and plates. *J. Geophys. Res.* **110**, D17203. (doi:10.1029/2005JD005811)

34. Dang C, Fu Q, Warren SG. 2016 Effect of snow grain shape on snow albedo. *J. Atmos. Sci.* **73**, 3573–3583. (doi:10.1175/JAS-D-15-0276.1)

35. LaChapelle ER. 1969 *Field guide to snow crystals*. Seattle, WA: University of Washington Press.

36. Kokhanovsky AA, Zege EP. 2004 Scattering optics of snow. *Appl. Opt.* **43**, 1589–1602. (doi:10.1364/AO.43.001589)

37. O'Brien H, Munis RH. 1975 *Red and near-infrared spectral reflectance of snow*. US Army CRREL Research Report 332. Hanover, NH: US Army Cold Regions Research and Engineering Laboratory.

38. Brandt RE, Warren SG, Worby AP, Grenfell TC. 2005 Surface albedo of the Antarctic sea-ice zone. *J. Clim.* **18**, 3606–3622. (doi:10.1175/JCLI3489.1)

39. Mullen PC, Warren SG. 1988 Theory of the optical properties of lake ice. *J. Geophys. Res.* **93**, 8403–8414. (doi:10.1029/JD093iD07p08403)

40. Weeks WF, Ackley SF. 1982 *The growth, structure, and properties of sea ice*. CRREL Monograph 82–1. Hanover, NH: Cold Regions Research and Engineering Laboratory.

41. Maykut GA, Light B. 1995 Refractive-index measurements in freezing sea-ice and sodium chloride brines. *Appl. Opt.* **34**, 950–961. (doi:10.1364/AO.34.000950)

42. Light B, Maykut GA, Grenfell TC. 2004 A temperature-dependent, structural-optical model of first-year sea ice. *J. Geophys. Res.* **109**, C06013. (doi:10.1029/2003JC002164)

43. Light B, Grenfell TC, Perovich DK. 2008 Transmission and absorption of solar radiation by Arctic sea ice during the melt season. *J. Geophys. Res.* **113**, C03023. (doi:10.1029/2006JC003977)

44. Morgan VI. 1972 Oxygen isotope evidence for bottom freezing on the Amery Ice Shelf. *Nature* **238**, 393–394. (doi:10.1038/238393a0)

45. Warren SG, Roesler CS, Morgan VI, Brandt RE, Goodwin ID, Allison I. 1993 Green icebergs formed by freezing of organic-rich seawater to the base of Antarctic ice shelves. *J. Geophys. Res.* **98**, 6921–6928. (doi:10.1029/92JC02751)

46. Warren SG, Roesler CS, Morgan VI, Brandt RE, Goodwin ID, Allison I. 1993 Correction to 'Green icebergs formed by freezing of organic-rich seawater to the base of Antarctic ice shelves' by S.G. Warren *et al*. *J. Geophys. Res.* **98**(C10), 18309. (doi:10.1029/93JC01904)

47. Whillans IM, Cassidy WA. 1983 Catch a falling star: meteorites and old ice. *Science* **222**, 55–57. (doi:10.1126/science.222.4619.55)

48. Harvey RP, Dunbar NW, McIntosh WC, Esser RP, Nishiizumi K, Taylor S, Caffee MW. 1998 Meteoritic event recorded in Antarctic ice. *Geology* **26**, 607–610. (doi:10.1130/0091-7613(1998)026<0607:MERIAI>2.3.CO;2)

49. Voosen P. 2017 2.7-million-year-old ice opens window on past. *Science* **357**, 630–631. (doi:10.1126/science.357.6352.630)

50. Dadic R, Mullen PC, Schneebeli M, Brandt RE, Warren SG. 2013 Effects of bubbles, cracks, and volcanic tephra on the spectral albedo of bare ice near the Trans-Antarctic Mountains: implications for sea-glaciers on Snowball Earth. *J. Geophys. Res.* **118**, 1658–1676. (doi:10.1002/jgrf.20098)

51. Hudson SR, Warren SG, Brandt RE, Grenfell TC, Six D. 2006 Spectral bidirectional reflectance of Antarctic snow: measurements and parameterization. *J. Geophys. Res.* **111**, D18106. (doi:10.1029/2006JD007290)

52. Warren SG, Roesler CS, Brandt RE, Curran M. 2019 Green icebergs revisited. *J. Geophys. Res.* (*Oceans*) **124**, 14pp (Early View). (doi:10.1029/2018JC014479)

53. Loeb NG. 1997 In-flight calibration of NOAA AVHRR visible and near-IR bands over Greenland and Antarctica. *Int. J. Remote Sens.* **18**, 477–490. (doi:10.1080/014311697218908)

54. Masonis SJ, Warren SG. 2001 Gain of the AVHRR visible channel as tracked using bidirectional reflectance of Antarctic and Greenland snow. *Int. J. Remote Sens.* **22**, 1495–1520. (doi:10.1080/01431160121039)

55. Grenfell TC, Warren SG, Mullen PC. 1994 Reflection of solar radiation by the Antarctic snow surface at ultraviolet, visible, and near-infrared wavelengths. *J. Geophys. Res.* **99**, 18 669–18 684. (doi:10.1029/94JD01484)

56. Armstrong T, Roberts B, Swithinbank C. 1973 *Illustrated glossary of snow and ice*. Cambridge, UK: Scott Polar Research Institute.

57. Leroux C, Fily M. 1998 Modeling the effect of sastrugi on snow reflectance. *J. Geophys. Res.* **103**, 25 779–25 788. (doi:10.1029/98JE00558)

58. Warren SG, Brandt RE, Hinton PO. 1998 Effect of surface roughness on bidirectional reflectance of Antarctic snow. *J. Geophys. Res.* (*Planets*) **103**, 25 789–25 807. (doi:10.1029/98JE01898)

59. Hudson SR, Warren SG. 2007 An explanation for the effect of clouds over snow on the top-of-atmosphere bidirectional reflectance. *J. Geophys. Res.* **112**, D19202. (doi:10.1029/2007JD008541)

60. Warren SG, Wiscombe WJ. 1980 A model for the spectral albedo of snow. II: Snow containing atmospheric aerosols. *J. Atmos. Sci.* **37**, 2734–2745. (doi:10.1175/1520-0469(1980)037<2734:AMFTSA>2.0.CO;2)

61. Dang C, Brandt RE, Warren SG. 2015 Parameterizations for narrowband and broadband albedo of pure snow, and snow containing mineral dust and black carbon. *J. Geophys. Res.* (*Atmospheres*) **120**(11), 5446–5468. (doi:10.1002/2014JD022646)

62. Warren SG. 2019 Light-absorbing impurities in snow: a personal and historical account. *Front. Earth Sci.* **6**, art. 250 (8 pp.). (doi:10.3389/feart.2018.00250)

63. Cornell RM, Schwertmann U. 2003 *The iron oxides*, 2nd edn. Weinheim, Germany: VCH.

64. Babin M, Stramski D. 2004 Variations in the mass-specific absorption coefficient of mineral particles suspended in water. *Limnol. Oceanogr.* **49**, 756–767. (doi:10.4319/lo.2004.49.3.0756)

65. Clarke AD, Noone KJ. 1985 Soot in the Arctic snowpack: a cause for perturbations in radiative transfer. *Atmos. Environ.* **19**, 2045–2053. (doi:10.1016/0004-6981(85)90113-1)

66. Doherty SJ, Warren SG, Grenfell TC, Clarke AD, Brandt RE. 2010 Light-absorbing impurities in Arctic snow. *Atmos. Chem. Phys.* **10**, 11 647–11 680. (doi:10.5194/acp-10-11647-2010)

67. Doherty SJ, Dang C, Hegg DA, Zhang R, Warren SG. 2014 Black carbon and other light-absorbing particles in snow of central North America. *J. Geophys. Res.* **119**, 12 807–12 831. (doi:10.1002/2014JD022350)

68. Wang X, Doherty SJ, Huang J. 2013 Black carbon and other light-absorbing impurities in snow across northern China. *J. Geophys. Res.* (*Atmos.*) **118**, 1471–1492. (doi:10.1029/2012JD018291)

69. Ye H, Zhang R, Shi J, Huang J, Warren SG, Fu Q. 2012 Black carbon in seasonal snow across northern Xinjiang in northwestern China. *Environ. Res. Lett.* **7**, 044002. (doi:10.1088/1748-9326/7/4/044002)

70. Warren SG, Clarke AD. 1990 Soot in the atmosphere and snow surface of Antarctica. *J. Geophys. Res.* **95**, 1811–1816. (doi:10.1029/JD095iD02p01811)

71. Zatko MC, Warren SG. 2015 East Antarctic sea ice in spring: spectral albedo of snow, nilas, frost flowers, and slush; and light-absorbing impurities in snow. *Ann. Glaciol.* **56**, 53–64. (doi:10.3189/2015AoG69A574)

72. Hori M *et al.* 2006 In-situ measured spectral directional emissivity of snow and ice in the 8–14 μm atmospheric window. *Remote Sens. Environ.* **100**, 486–502. (doi:10.1016/j.rse.2005.11.001)

73. Dozier J, Warren SG. 1982 Effect of viewing angle on the infrared brightness temperature of snow. *Water Resour. Res.* **18**, 1424–1434. (doi:10.1029/WR018i005p01424)

74. Wald AE. 1994 Modeling thermal infrared (2–14 μm) reflectance spectra of frost and snow. *J. Geophys. Res.* (*Solid Earth*) **99**, 24 241–24 250. (doi:10.1029/94JB01560)

75. Wiscombe WJ. 1980 Improved Mie scattering algorithms. *Appl. Opt.* **19**, 1505–1509. (doi:10.1364/AO.19.001505)

76. Hori M, Aoki T, Tanikawa T, Hachikubo A, Sugiura K, Kuchiki K, Niwano, M. 2013 Modeling angular-dependent spectral emissivity of snow and ice in the thermal infrared atmospheric window. *Appl. Opt.* **52**, 7243–7255. (doi:10.1364/AO.52.007243)

77. Lubin D, Massom RA. 2006 *Polar remote sensing*, Vol. 1, *Atmosphere and oceans*. Chichester, UK, and Berlin, Germany: Praxis/Springer.

78. Massom RA, Lubin D. 2006 *Polar remote sensing*, Vol. 2, *Ice sheets*. Chichester, UK, and Berlin, Germany: Praxis/Springer.

79. Nolin AW. 2010 Recent advances in remote sensing of seasonal snow. *J. Glaciol.* **56**, 1141–1150. (doi:10.3189/002214311796406077)

80. Dumont M, Gascoin S. 2016 Optical remote sensing of snow cover. In *Land surface remote sensing in continental hydrology* (eds N Baghdadi, M Zribi), chapter 4, pp. 115–137. Amsterdam, The Netherlands: ISTE Press, Elsevier. (doi:10.1016/C2015-0-01226-6)

81. Gloersen P, Campbell WJ, Cavalieri DJ, Comiso JC, Parkinson CL, Zwally HJ. 1992 *Arctic and Antarctic sea ice, 1978–1987: satellite passive-microwave observations and analysis*. NASA SP-511. Washington, DC: National Aeronautics and Space Administration.

82. Steffen K, Nghiem SV, Huff R, Neumann G. 2004 The melt anomaly of 2002 on the Greenland Ice Sheet from active and passive microwave satellite observations. *Geophys. Res. Lett.* **31**, L20402. (doi:10.1029/2004GL020444)

83. Hoekstra P, Cappillino P. 1971 Dielectric properties of sea and sodium chloride ice at UHF and microwave frequencies. *J. Geophys. Res.* **76**, 4922–4931. (doi:10.1029/JB076i020p04922)

84. Bogorodsky V, Bentley C, Gudmandsen P. 1985 *Radioglaciology*. Dordrecht, The Netherlands: D. Reidel.

85. Brandt RE, Warren SG, Clarke AD. 2011 A controlled snowmaking experiment testing the relation between black carbon content and reduction of snow albedo. *J. Geophys. Res.* **116**, D08109. (doi:10.1029/2010JD015330)

86. Hadley OL, Kirchstetter TW. 2012 Black-carbon reduction of snow albedo. *Nature Clim. Change* **2**, 437–440. (doi:10.1038/nclimate1433)

87. Ackerman TP, Toon OB. 1981 Absorption of visible radiation in atmosphere containing mixtures of absorbing and nonabsorbing particles. *Appl. Opt.* **20**, 3661–3668. (doi:10.1364/AO.20.003661)

88. Yallop ML *et al.* 2012 Photophysiology and albedo-changing potential of the ice algal community on the surface of the Greenland ice sheet. *ISME J.* **6**, 2302–2313. (doi:10.1038/ismej.2012.107)

89. Stibal M *et al.* 2017 Algae drive enhanced darkening of bare ice on the Greenland ice sheet. *Geophys. Res. Lett.* **44**, 11 463–11 471. (doi:10.1002/2017GL075958)